

PAPER • OPEN ACCESS

Reactive ion beam figuring of optical aluminium surfaces

To cite this article: Jens Bauer *et al* 2017 *J. Phys. D: Appl. Phys.* **50** 085101

View the [article online](#) for updates and enhancements.

You may also like

- [Black silicon method X: a review on high speed and selective plasma etching of silicon with profile control: an in-depth comparison between Bosch and cryostat DRIE processes as a roadmap to next generation equipment](#)
H V Jansen, M J de Boer, S Unnikrishnan et al.
- [Universal pattern transfer methods for metal nanostructures by block copolymer lithography](#)
Kun-Hua Tu, Wubin Bai, George Lontos et al.
- [A Blazed Si Grating for Soft X-Ray Fabricated by Two-Stage Reactive Ion-Beam Etching](#)
Hiroaki Aritome, Toshiya Yamato, Shinji Matsui et al.

ECS Toyota Young Investigator Fellowship

For young professionals and scholars pursuing research in batteries, fuel cells and hydrogen, and future sustainable technologies.

At least one \$50,000 fellowship is available annually.
More than \$1.4 million awarded since 2015!



Application deadline: January 31, 2023



TOYOTA

Learn more. Apply today!

Reactive ion beam figuring of optical aluminium surfaces

Jens Bauer¹, Frank Frost and Thomas Arnold

Leibniz Institute of Surface Modification (IOM), Permoserstrasse 15, D-04318 Leipzig, Germany

E-mail: jens.bauer@iom-leipzig.de

Received 2 August 2016, revised 30 September 2016

Accepted for publication 12 October 2016

Published 30 January 2017



Abstract

Ultra-smooth and arbitrarily shaped reflective optics are necessary for further progress in EUV/XUV lithography, x-ray and synchrotron technology. As one of the most important technological mirror optic materials, aluminium behaves in a rather difficult way in ultra-precision machining with such standard techniques as diamond-turning and subsequent ion beam figuring (IBF). In particular, in the latter, a strong surface roughening is obtained. Hence, up to now it has not been possible to attain the surface qualities required for UV or just visible spectral range applications. To overcome the limitations mainly caused by the aluminium alloy structural and compositional conditions, a reactive ion beam machining process using oxygen process gas is evaluated. To clarify the principle differences in the effect of oxygen gas contrary to oxygen ions on aluminium surface machining, we firstly focus on chemical-assisted ion beam etching (CAIBE) and reactive ion beam etching (RIBE) experiments in a phenomenological manner. Then, the optimum process route will be explored within a more quantitative analysis applying the concept of power spectral density (PSD) for a sophisticated treatment of the surface topography. Eventually, the surface composition is examined by means of dynamic secondary ion mass spectrometry (SIMS) suggesting a characteristic model scheme for the chemical modification of the aluminium surface during oxygen ion beam machining. Monte Carlo simulations were applied to achieve a more detailed process conception.

Keywords: ultra-precision surface machining, ion beam figuring, reactive ion beam etching, aluminium, mirrors


(Some figures may appear in colour only in the online journal)

1. Introduction

Shape-adapted optics are of increasing interest since high quality but compactly designed optical systems are a driving force in modern optical device development. Short-wavelength applications or operation in rough environmental conditions, i.e. with high thermal load or mechanical stress, require metal mirror optical systems. Typical fields of utilization are EUV/XUV lithography [1], x-ray and synchrotron optics. Since mirror optics can be designed with high strength and

low-weight, large-scale applications, e.g. telescope mirrors, are also relevant [2]. Aluminium is lightweight, cheap, and a good machinable material with outstanding optical properties since the reflection coefficient ranges from the UV to the IR spectral region with values well above 90%. Aluminium-based mirror optics with a customized shape, e.g. aspherical or freeform, bear a high potential in laser and illuminating engineering, as well as in advanced optical systems [3, 4].

The upcoming needs of greater flexible shape adjustment and increasing surface quality demand improved deterministic tools in ultra-precise surface machining [5, 6]. Ion beam figuring (IBF) is an established method in high-end surface manufacturing of fused silica, silicon, silicon carbide and low expansion glasses [7–12]. Advanced IBF techniques [13–16] and IBF machine optimization proposals [17] are under consideration. However, the direct machining of

 Original content from this work may be used under the terms of the [Creative Commons Attribution 3.0 licence](https://creativecommons.org/licenses/by/3.0/). Any further distribution of this work must maintain attribution to the author(s) and the title of the work, journal citation and DOI.

¹ Author to whom any correspondence should be addressed.

Table 1. Ion beam parameters and corresponding aluminium etch rates with respect to the process gas applied. For the purpose of qualitative comparison (section 1) between the RIBE (index 1) and the CAIBE experiments, the operating distance and the beam parameters were almost retained. In a second, more quantitative, analysis (sections 3.2/3.3) of the RIBE processes (index 2) the operating distance and beam parameters were adjusted. In particular, the operating distance denotes the optimum distance between the sample and ion source where the FWHM is small and the integral beam current is near its maximum.

Process mode	Operating gas	Process pressure (Pa)	FWHM (mm)	Beam current (mA)	Operating distance (mm)	Etch rate ($\text{mm}^3 \text{h}^{-1}$)
RIBE ¹	Ar : O ₂ (6 : 1)	5.0×10^{-3}	4.6	0.8	81	0.23
	Ar : O ₂ (15 : 1)	4.5×10^{-3}	4.6	0.8	81	0.45
	Ar : O ₂ (6 : 1)	5.0×10^{-3}	5.7	1.0	81	0.64
CAIBE	Ar : O ₂ (15 : 1)	4.5×10^{-3}	5.0	1.0	81	0.74
RIBE ²	O ₂	1.4×10^{-3}	5.1	2.4	22	0.17
	Ar : O ₂ (6 : 1)	5.0×10^{-3}	5.1	1.2	34	0.21
	Ar	4.0×10^{-3}	5.2	1.3	44	0.89

standard aluminium alloys (e.g. Al6061, Al905) have failed up to now, since distinct surface roughening is obtained during IBF processing with noble gases [18]. One technological solution is the coating of the aluminium device with an amorphous NiP layer [19]. NiP is well-shapeable and reveals ultra-smooth surfaces after machining with IBF. But the additional process steps in the fabrication of these optics are costly and time consuming. Moreover, the spectral reflection properties of NiP are not as good as pure aluminium surfaces. That is usually why a further metallization layer (e.g. Au, Ag) is needed on NiP-based optics. During application, additional issues arise, e.g. bending due to the bimetallic effect and NiP delamination [20, 21]. Hence, it would be most desirable to find an alternative figuring technique providing direct surface machining of technologically interesting aluminium alloys.

A promising route is a reactive ion beam etch (RIBE) process [22]. In addition to conventional IBF, the process gas contains chemically active species changing the etch mechanism from pure sputtering to a chemical-enhanced sputter etch process. Since the complexity of the etch process increases, ensuring process controllability is an important technological issue to provide precise surface machining. Usually aluminium dry etching rests upon chlorine-based chemistry [23], since aluminium chlorides are the only halide species which readily transfer into the gas phase. However, chlorine is highly reactive and is, from a technological point of view, filthy, producing hazardous process by-products and decreasing process stability and machine life-time due to the erosion of most materials in contact with it. This paper focuses on the RIBE machining of standard aluminium alloys with oxygen-containing process gas. In contrast to the classical RIBE scheme, no volatile process products are generated by the reactive gas species but the machined surface is particularly chemically modified. As a result, a very stable and non-hazardous etch mechanism is obtained which, to the best of our knowledge, has never been applied for ion erosion technology so far. The etch behaviour is analysed with a special focus on the surface topography and the local chemical modification. Supported by Monte Carlo simulations, the experimental examinations are summarized within a phenomenological RIBE process scheme.

2. Experimental

Ion beam machining experiments were performed in a vacuum chamber with a base pressure of 2×10^{-5} Pa. The ion beam was generated by a transformer-coupled plasma ion source (13.56 MHz) with a focusing triple grid extraction system with an opening diameter of 10 mm. The sample holder was attached to a five-axes motion system allowing a deterministic movement in front of the ion beam. To reduce the thermal effects during processing, the sample holder exhibited a water-cooled sample mounting to provide an efficient heat dissipation from the sample. For *in situ* beam analysis, a Faraday cup was integrated into the sample holder. We used Ar (N5.2) and O₂ (N5.1) as well as argon–oxygen gas mixtures for ion generation. At 1.5 kV beam-voltage, a well-shaped Gaussian-type ion beam profile was obtained for all process gases. For chemical-assisted ion beam etching (CAIBE) experiments, an additional gas inlet into the chamber allowed for a background gas supply to be directed towards the sample at an operating distance of 81 mm. The optimized ion beam process parameters used for the ion beam machining experiments are summarized in table 1. The Gaussian-type beam profile is characterized by the full-width half maximum (FWHM) and the integral beam current. For etch rate determination, homogeneous inverse top hat profiles were prepared by scanned ion beam machining over a graphite hard mask.

Aluminium disc samples with a 47 mm diameter were made from the rapidly solidified aluminium alloy materials Al6061 and Al905 (RSP Technology) [24, 25]. The diamond-turned surfaces were cleaned with acetone prior to ion beam processing. A graphite hard mask with a 13 mm circular opening defined the testing field for the ion beam machining experiments. The ion beam was scanned s-like with a constant velocity of 1.5 mm s^{-1} and a line pitch of 0.5 mm over the mask opening to obtain a homogeneously etched area with defined step edges at the opening borders.

The sample topography was analysed by optical microscopy (Zeiss Axiotech 100), confocal microscopy (nanofocus μsurf), white light interferometry (WLI; ADE MicroXAM), and atomic force microscopy (AFM; Bruker Dimension

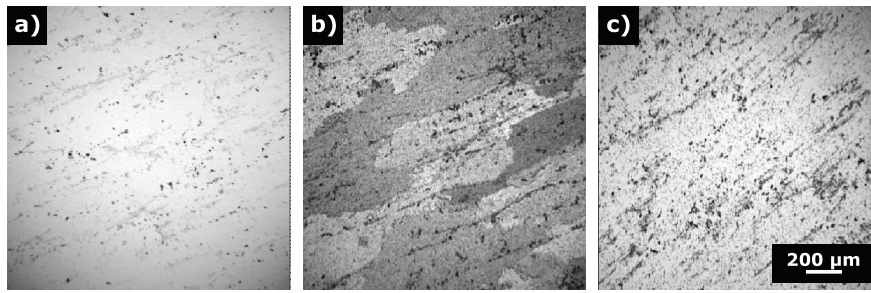


Figure 1. Surface morphology images by confocal microscopy of Al6061 samples, (a) untreated and after ion beam machining with (b) argon, and (c) oxygen gas supply.

ICON). For WLI, objectives with $10\times$ and $50\times$ magnification were used. The image sizes were $804\ \mu\text{m} \times 609\ \mu\text{m}$ and $162\ \mu\text{m} \times 122\ \mu\text{m}$, respectively, with an equal pixel resolution of 746×478 . The AFM was operated in tapping modeTM and in an xy-closed loop configuration. To measure the surface topography, the z-sensor signal was utilized. Scanning areas of $10\ \mu\text{m} \times 10\ \mu\text{m}$ and $1\ \mu\text{m} \times 1\ \mu\text{m}$ were used with a pixel resolution of 1024×1024 for each area. The two-dimensional power spectral density (PSD) was calculated from the topography images by the SPIP software (version 6.0.14 by Image Metrology). Then, a self-made MATLAB-based script was applied for radial integration resulting in the so-called isotropic PSD function. Note the deceptive nomenclature, since all anisotropic contributions are superposed to allow the discussion of the two-dimensional surface features within a single function. Surface composition mapping was performed by secondary-electron microscope energy dispersive x-ray (SEM-EDX) measurements in a Zeiss Gemini Ultra 55 machine with a Bruker XFlash 3001 detector. Depth profiling of the sample composition in the near surface region was monitored by dynamic time-of-flight secondary ion mass spectrometry (TOF-SIMS; IONTOF). Therefore a Cs-sputter source and a 15 keV Ga-ion analysis beam were used in negative ion detection mode. The $50\ \mu\text{m} \times 50\ \mu\text{m}$ field of analysis was centered within a $300\ \mu\text{m} \times 300\ \mu\text{m}$ sputter crater. The depth scalings of the SIMS profiles were linearly approximated from the crater depths measured by WLI.

Monte-Carlo simulations of the ion-surface interaction were performed using the SRIM-2008 (stopping and range of ions in matter) code within the SRIM/TRIM 2013 software [26], and the TRIM.SP (transport of ions in matter, sputtering version) code [27]. Both codes allow for the calculation of ion trajectories inside the solids to determine implantation profiles and full collision cascades for energy loss and sputtering yield analysis. In SRIM-2008, the ZBL interaction potential (universal potential proposed by Ziegler *et al* [28]) is used, while in TRIM.SP usually the Krypton–Carbon potential is applied [29]. For comparison reasons, the ZBL potential was also utilized in TRIM.SP for this study. However, the choice of the interaction potential indicated only marginal changes in the simulation output quantities: implantation depths and spreads varied within 5% between the ZBL and Krypton–Carbon potential. The calculated sputter yields showed no effect on

the interaction potential applied. All TRIM.SP simulations in this paper are made by application of the ZBL potential.

3. Results and discussion

3.1. Effect of oxygen process gas

In accordance with the previously reported results by Egert [18], our IBF experiments with argon ions also reveal a considerable surface degradation on aluminium substrates. Millimetre and sub-millimetre sized domain-patterns are formed exhibiting strongly differing surface roughness and height differences up to 90 nm between each other after 760 nm depth machining (figure 1(b)). Furthermore, microscopic etch pits are observed which contribute strongly to the micro-roughness. A significant improvement of the surface quality can be reached with pure oxygen processing (figure 1(c)). The domain-pattern structure is eliminated, but the defect structure in the form of a series of etch pits with a tendency of ordering inside directed chains over the surface is still apparent. In an optical inspection under grazing and under normal incidence the domain-patterns after argon processing result in a shaded, non-specular surface. By lowering the machining depth to about 400 nm, a more specular surface is observed, but a strong haze already dominates. In contrast, after 400 nm oxygen processing, a highly specular surface with only suggestive portions of haze is obtained and the aluminium surface color is maintained. However, by increasing the machining depth, the haziness increases, but usually most figure errors, which need to be corrected in mirror finishing, are well covered by the 400 nm depth range.

The effect of oxygen is further analyzed by ion beam machining experiments with argon–oxygen gas mixtures (figure 2). The argon flow is kept constant. To explore the difference between energetic oxygen ions and non-activated molecular oxygen gas, two experimental situations are distinguished: (1) The CAIBE process: the ion beam is driven by argon gas only. Oxygen is supplied directly into the chamber while the oxygen flow is oriented towards the sample surface. Hence, the oxygen interacts molecularly with the aluminium surface. (2) The RIBE process: argon and oxygen are both supplied into the ion source to produce an ion beam mixed with both argon ions and oxygen ions.

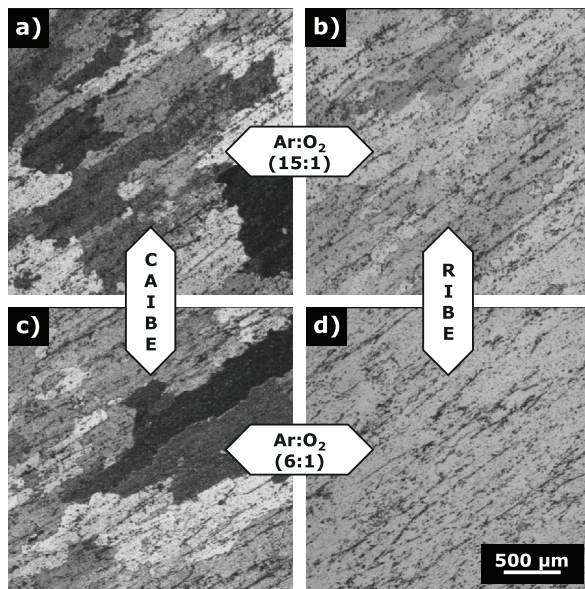


Figure 2. Surface morphology images by optical microscopy of Al6061 samples after CAIBE and RIBE processing with different argon–oxygen compositions.

The surface morphology after the CAIBE process (figure 2(a)/(c)) shows the domain-pattern structure similar to the situation without oxygen background gas (figure 1(b)). Besides, no significant effect of the oxygen flow rate is seen. In the case of RIBE processing, the domain-pattern structure formation is strongly reduced (figure 2(b)) and with a higher oxygen flow it can be completely eliminated (figure 2(d)). However, in all cases the ordered etch pit structures are distinctly apparent.

As a result, a sufficient diluted oxygen flow as $\text{Ar} : \text{O}_2 = 6 : 1$ allows a strong improvement in the aluminium surface quality during ion beam machining in the RIBE process scheme. This observation is opposite to previously reported work by Bernheim and Slodzian [30], where a surface improvement was achieved with an oxygen addition to the background gas, while an oxygen addition to the argon gas supply for ion beam processing behaved less effectively. From molecular oxygen in the background gas, the ready formation of a native oxide layer can be assumed. However, our results suggest that it is necessary that energetic ionized oxygen particles interact with the aluminium surface. Also in this case, a surface oxide formation has to be considered. This view is supported by a significant drop of the etch rate by a factor of 4–5 in the case of oxygen-assisted ion beam machining (table 1). Note the similar beam currents in argon and argon–oxygen processing. In accordance, the argon sputtering yield of an oxidized aluminium surface is found to be about four times lower compared to pure aluminium [30]. This characteristic is also a severe issue in the reactive sputter deposition of alumina thin films called substrate poisoning [31].

In the Al6061 alloy material used for the experiments, Si, Mg, and Cu portions are added to the aluminium base. The local composition distribution after RIBE processing was monitored by SEM–EDX mapping. As a remarkable result, significant Si and Mg fractions are found to be accumulated together within the etch pits (figure 3). Indeed, quaternary

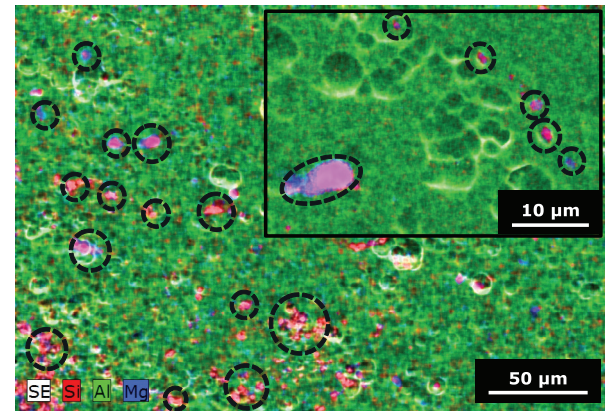


Figure 3. SEM–EDX mapping images of an $\text{Ar} : \text{O}_2 (6 : 1)$ -processed Al6061 sample with an etch depth of $2 \mu\text{m}$ revealing Si- and Mg-rich precipitates within the etch pits.

precipitates with $\text{Al}_5\text{Cu}_2\text{Mg}_8\text{Si}_6$ stoichiometry are reported to be formed within the Al6061 matrix during the initial alloy annealing procedure [32]. The etch pit formation is strongly promoted by the inhomogeneous matrix structure. The etch pits are assumed to result from the preferential sputter erosion of the precipitates. Once an etching pit has formed its topography, it is persistently conserved during the progress of the ion beam machining process. A temporal analysis of the surface morphology revealed an increasing etch pit surface density with the RIBE process time. Furthermore, the lateral pit size enlarges due to isotropic etching contributions and coagulation of neighbouring etch pits. Since the precipitates are statistically distributed inside the alloy matrix, continuous new etch pits are formed during increasing etch depth. As a result, the surface quality declines progressively. However, the etching rates were steadfastly stable during each ion beam machining process scheme considered.

The precipitate grains in the Al6061 alloy also adversely affect the diamond turning process, which was the previous process step in the optics fabrication process chain before ion beam machining. As seen from the WLI analysis (figure 4(a)) micron sized particles are detached out of the surface leaving surface pits and the counter-clockwise dropped particles as a result of the turning process. Hence, the aluminium surface, which is generally dominated by about 12 nm high and $13 \mu\text{m}$ spaced turning marks, is further declined by those surface pit-particle couples prior to ion beam machining. As a rude measure of the surface roughness in the mid spatial frequency range, root-mean-square (rms) roughness values are determined from the measured WLI images. The roughness before ion beam machining is about $(6.2 \pm 1.6) \text{ nm}$ for Al6061. In order to avoid inhomogeneous matrix structure effects, an alternative alloy material was tested. Al905 does not contain Si and Mg, but contains Fe, Cu, and Mn instead. The surface quality before ion beam treatment is already better for this alloy, since no detached particles from the diamond turning process are apparent (figure 4(c)). The surface topography is determined by the turning marks only exhibiting the same geometry but less pronounced edges as on the investigated Al6061 surfaces. For the Al905 surfaces, the roughness amounts to about

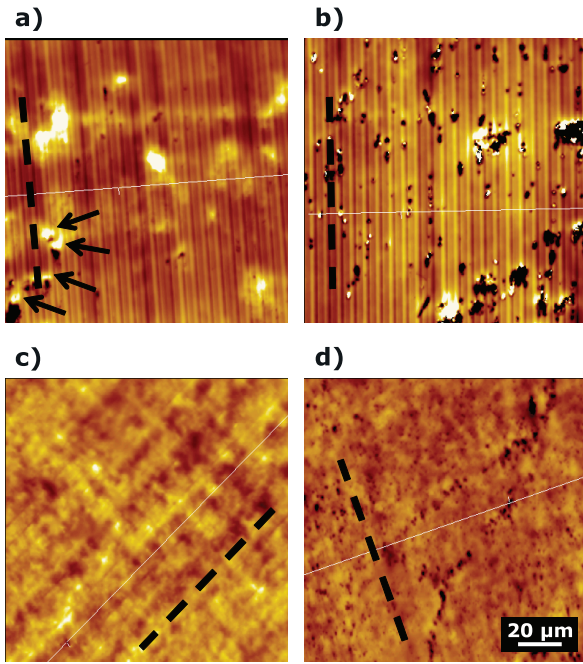


Figure 4. WLI topography images (50 \times objective) of Al6061 and Al905 samples before (left) and after (right) RIBE machining with oxygen process gas. The etching depths were (b) 400 nm and (d) 380 nm. The dotted lines indicate the direction of the turning marks. The arrows in (a) point at the surface pit-particle couples. (a) Al6061 untreated. (b) Al6061 after RIBE. (c) Al905 untreated. (d) Al905 after RIBE.

(5.5 \pm 0.4) nm. The qualitative differences between the two materials become apparent after oxygen ion beam machining (figure 4(b)/(d)). Note, the etch rates for IBF and RIBE are as given in table 1 for both materials. After RIBE the roughness values increase to (14.0 \pm 2.2) nm and (6.8 \pm 0.5) nm for Al6061 and Al905, respectively. For both materials the initial surface topography is preserved after 400 nm depth etching so far. In particular, the turning marks still remain with their initial height, but with smoothed edges. The stronger roughness increase for Al6061 is mainly caused by the etch pits formed with a size in the range of a few microns. However, also on the Al905 surfaces, the formation of surface pits is observed. Their size is in the sub-micrometre range and thus smaller than on Al6061. In summary, the best surface improvement is obtained for the Al905 material. The forthcoming topics are thus limited to Al905 only.

3.2. Quantitative topography analysis

Generally, the sample topography is composed of various surface regimes on different length scales, i.e. primary shape, waviness, roughness, and micro-roughness. Each regime contributes in a specific manner to the optical surface characteristics: (1) The primary shape defines the light beam shaping properties; (2) the waviness allows control over light diffraction; (3) the roughness and micro-roughness defines the diffusive or reflective appearance. For mirror optics, typically a low roughness is necessary to reach high reflection properties. A common measure for the surface roughness is the rms

deviation of the overall surface form from which the primary surface shape and the waviness has to be subtracted. The measurement result depends strongly on the data evaluation routine. Often the surface shape is assumed to be a standard geometrical form (plate, cylinder, sphere) or a smoothing or fitting algorithm is applied to estimate long-wavelength structures. Since the actual surface shape and waviness are usually not known, these procedures can bear a great contribution to the systematic measuring faults. Another general problem is the systematic measuring faults from incorrectly represented surface features in the low-frequency and the high-frequency spatial range caused by the maximum image size and the limited resolution, respectively. Most data evaluation software tools do not account for this issue. Hence, surface roughness values usually differ for various measurement techniques and should be considered carefully.

The PSD allows a much better access to the surface characteristics providing the direct representation of the different surface regime contributions with respect to their spatial frequencies [33–35]. The surface roughness can be calculated from the isotropic PSD data via equation (1):

$$R_q(t) = \sqrt{\int_{f_{ll}}^{f_{ul}} 2\pi f \cdot \text{PSD}(f, t) df}. \quad (1)$$

The lower limit integral boundary $f_{ll} = 1/\lambda_c$ is given by the roughness cut-off wavelength λ_c indicating the transition to the surface waviness regime. The upper limit integral boundary $f_{ul} = 1/\lambda_s$ corresponds to the transition wavelength to micro-roughness λ_s , where the surface features turn from pseudo-periodic to a rather stochastic ordering. However, the transitions are not sharply separated and the cut-off frequencies cannot be specified within rigid rules. The major reasons are: (1) With regards to optical applications, micro-roughness features may also have a considerable impact on light scattering and thus loss of optical performance of the reflective element. (2) On the other hand, waviness but also pseudo-periodic features from the roughness regime may cause diffractive effects influencing the spectral reflection characteristics. (3) In general, light diffraction as well as scattering depend strongly on the light wavelength range of interest. Hence, the specific application has to be considered for definition of the cut-off wavelengths. Typical spatial frequency ranges for IR, VIS, and UV applications are labelled in figure 5. The upper limit is held constant to account for the overall micro-roughness contribution on the broad halo light scattering effects [33].

To measure the broad spatial frequency spectrum from the low over mid to the high frequency range, the combination of different measurement techniques is necessary. Thus, the PSD plots shown in figure 5 are composed of partial curves derived from differently sized AFM and WLI measurements, as shown in figure 6. To account for local topography changes, each measurement has been performed five times under the same conditions. The PSD plots in figure 5 are averaged and the given error bars represent the statistical standard deviations. Because of limitations in image size and resolution for each topography measurement technique, a careful analysis of the reliable spatial frequency range has to be carried out. Hence, each partial PSD is restricted to a specific spatial frequency

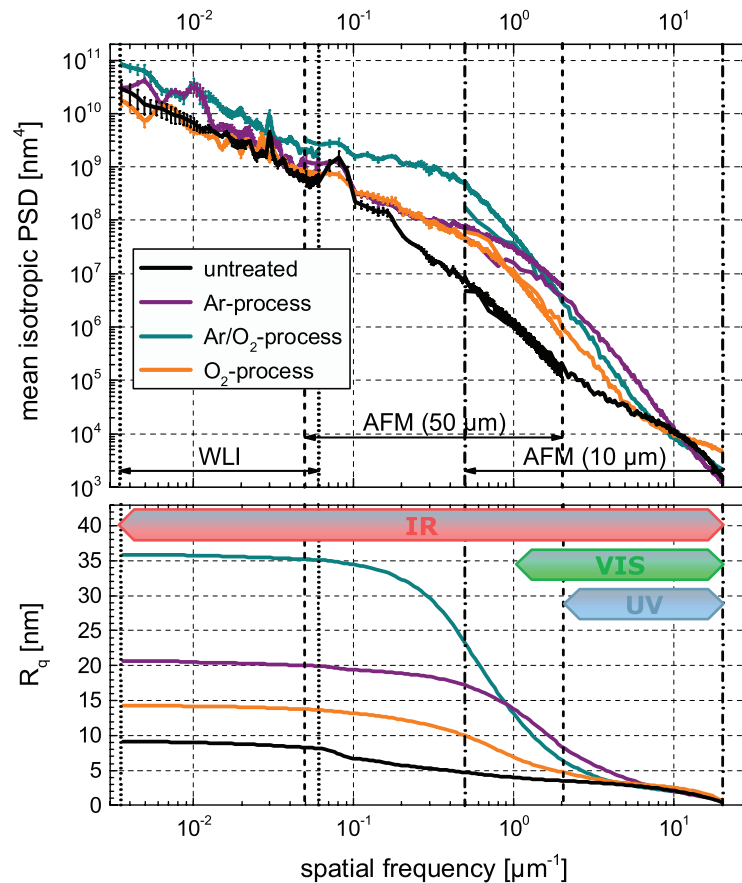


Figure 5. PSD spectra (top) before and after RIBE machining with different process gases on Al905 samples. The roughness spectra (bottom) are calculated by partial integration from the actual spatial frequency to $f_{ul} = 20.0 \mu\text{m}^{-1}$ via equation (1).

range, which is naturally not equivalent to the whole spatial frequency range provided by pure image data processing.

Almost in the whole spectral wavelength range no reduction of the PSD due to ion beam processing is found, i.e. the predefined surface topography is either kept equal or increased. However, there is one exception: the bump at $0.08 \mu\text{m}^{-1}$ correlates to a spatial wavelength of about $13 \mu\text{m}$. This feature reflects the diamond turning marks which are considerably smoothed out by any of the applied ion beam machining processes.

The deviation of the PSD spectra after processing to the PSD spectrum of the untreated case is a measure for the surface degradation with respect to the spatial frequency. Hence, strong PSD deviations can be correlated to topography features. The topography after argon processing is dominated by a strong roughening of the sample surface (see figure 6(b)). In contrast, ion beam machining with oxygen gas reveals a rather smooth surface, but shows the formation of sub-micron etch pits (figure 6(d)). The strongest surface degradation is obtained with the argon–oxygen gas mixture, since both a rough surface and etch pits with sizes up to a few microns are formed. As a consequence, the PSD deviation (figure 5) after argon–oxygen processing is significantly increased almost over the whole spatial frequency range up to about $7 \mu\text{m}^{-1}$, where the PSD curves merge. A maximum deviation

of about 2 dec is obtained in the mid frequency range at about $0.5 \mu\text{m}^{-1}$, correlating to the strong etch pit formation. The PSD deviation of the oxygen process is negligible in the low to mid frequency range until $0.1 \mu\text{m}^{-1}$. Hence, there seem to be no significant figure and waviness machining errors. In the range between $0.1 \mu\text{m}^{-1}$ and $5 \mu\text{m}^{-1}$, there is a stronger deviation with a maximum of about 1 dec at about $0.8 \mu\text{m}^{-1}$ which is a result of the individual and coalesced etch pits. Another deviation develops above $10 \mu\text{m}^{-1}$ which must be correlated to topography features with a size below 100nm . Argon processing reveals, to some extent, deviations in the low frequency range, but a strong deviation in the mid range between $0.1 \mu\text{m}^{-1}$ and $10 \mu\text{m}^{-1}$. The maximum deviation is situated around $1 \mu\text{m}^{-1}$ for about 1.5 dec resulting from the strong surface roughening.

The surface roughness plots in figure 5 are determined via equation (1) choosing the actual spatial frequency as the lower limit integral boundary and the maximum spatial frequency of $20.0 \mu\text{m}^{-1}$ as the upper limit integral boundary. In this way, the roughness value, which is decisive for the specific light wavelength range of the application, can be directly read from the roughness plots. The roughness values for the marked spectral ranges in figure 5 are summarized in table 2. As already indicated by the PSD characteristics, the roughness after oxygen ion beam machining is the

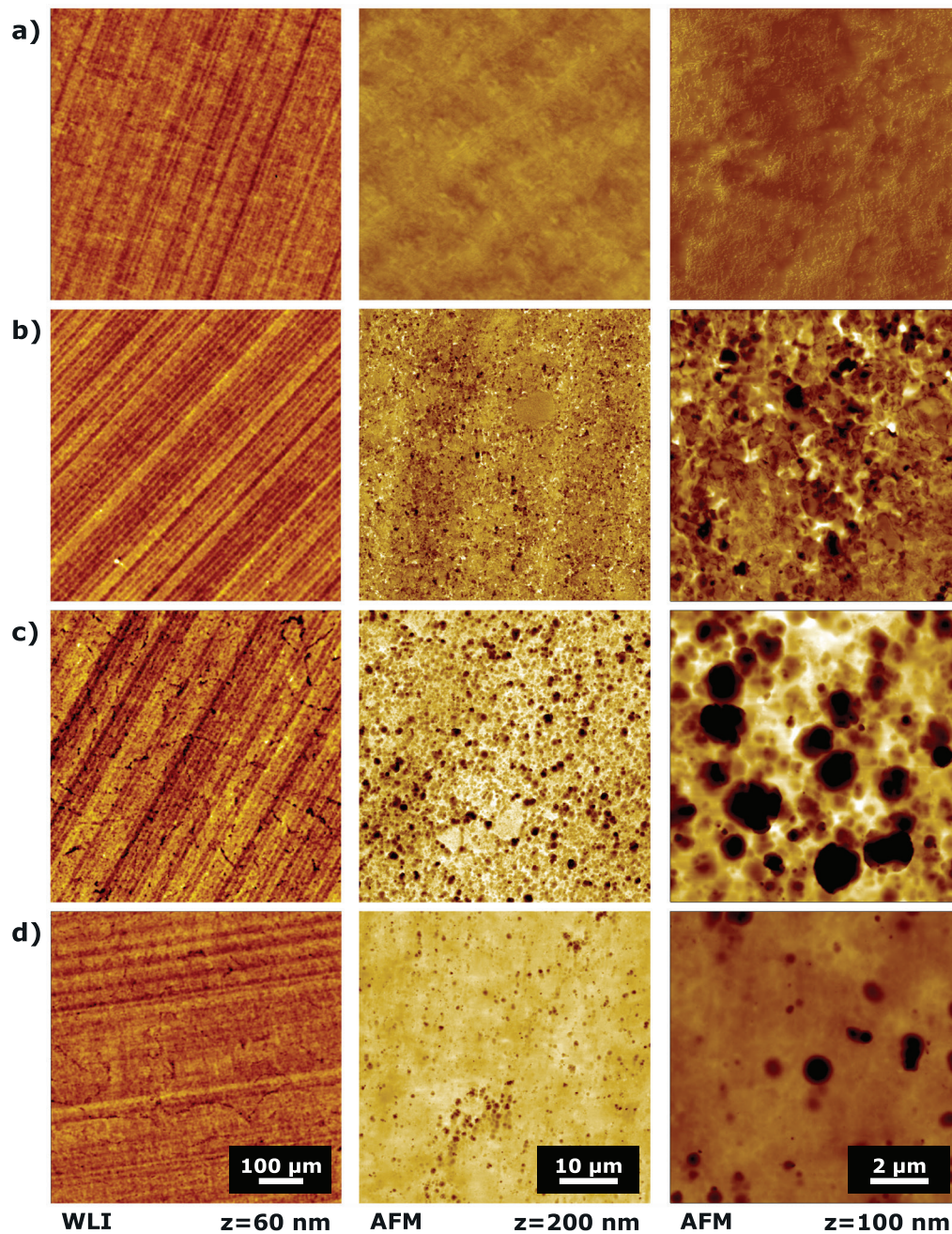


Figure 6. WLI (10× objective) and AFM topography images of Al905 samples, (a) untreated and after ion beam machining with (b) argon, (c) argon–oxygen, and (d) oxygen. The etching depth is about 380 nm for the three processes. The image height scale is indicated by the z -value.

lowest. In both cases where argon is involved, the roughness is evidently increased. But since a surface smoothing is not obtained anyway, it has to be stated that the initial surface quality before ion beam machining is crucial for the process result. Generally, the roughness deviation between any of the ion beam machining processes and the untreated case is enhanced with respect to the light wavelength range of interest from UV over VIS to the IR spectral region. This trend results from the strong PSD deviations in the mid spatial wavelength range. Nevertheless, comparing the oxygen RIBE process with the standard argon IBF process, it can be seen that all roughness deviations to the untreated case are considerably improved.

Table 2. Roughness values R_q with respect to the spectral range of interest (see labels in figure 5).

Etching process	UV (nm)	VIS (nm)	IR (nm)
Untreated	(3.5 ± 0.3)	(4.0 ± 0.4)	(9.2 ± 1.4)
O ₂	(4.8 ± 0.4)	(6.9 ± 0.6)	(14.3 ± 1.6)
Ar/O ₂	(6.5 ± 0.5)	(13.1 ± 0.7)	(35.9 ± 3.5)
Ar	(8.4 ± 0.7)	(13.8 ± 1.0)	(20.7 ± 1.9)

3.3. Chemical surface modification

The interaction region of the ion beam with the sample surface was analyzed by TOF-SIMS experiments applying the same

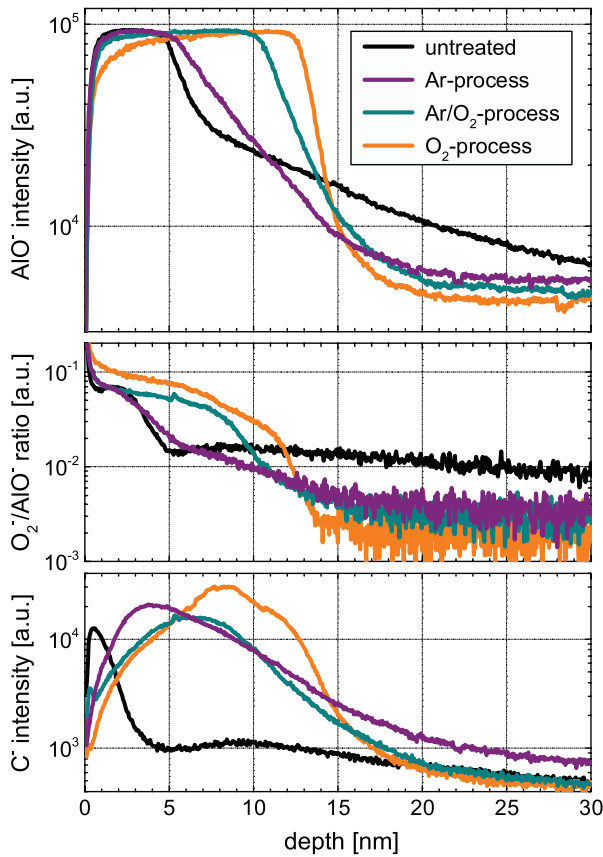


Figure 7. TOF-SIMS depth profiles after ion beam machining with different process gases on Al905 samples. The extent of the surface oxide layer is represented by the AlO^- signal (top). The $\text{O}_2^-/\text{AlO}^-$ signal ratio (middle) reveals stoichiometry changes within the oxide. Within the oxide layer an increased C^- signal (bottom) was found.

samples as depicted in figure 6 with 380 nm etch depth. Note, a native oxide layer of about 5 nm thickness is formed instantaneously during contact of a pure aluminium surface with air. To reduce the temporal effects, the SIMS measurements were performed directly after ion beam processing. However, this time the samples were exposed to air. Hence, the existence of a surface oxide layer has to be expected not only on the oxygen ion beam machined samples, but also on the untreated and oxygen-free processed samples.

The AlO^- -signal was used to illustrate the extent of the surface oxide layer (figure 7). The oxide layer thickness was determined as the distance from the surface to the depth, where the AlO^- -signal decreases to its half maximum value (table 3). As a measure for the interface sharpness between oxide and aluminium the slope of the AlO^- -signal was additionally determined at this depth. As major impacts on the interface sharpness, the abruptness of the compositional change and contributions from the micro-roughness have to be considered in the SIMS data evaluation. Since high-spatial frequency fractions of the PSD are most relevant for micro-roughness, the UV roughness values in table 2 are taken for a qualitative discussion.

The untreated sample revealed a native oxide thickness of about 5.7 nm. After argon IBF processing the oxide layer

Table 3. SIMS measurement results for the differently processed Al905 samples.

Etching process	Oxide layer thickness (nm)	Oxide/Al interface sharpness (dec nm^{-1})
Untreated	(5.7 ± 0.1)	(0.211 ± 0.004)
O_2	(13.0 ± 0.1)	(0.453 ± 0.004)
Ar/ O_2	(11.3 ± 0.1)	(0.213 ± 0.001)
Ar	(7.3 ± 0.1)	(0.1121 ± 0.0005)

is slightly enlarged to about 7.3 nm. However, the interface sharpness is significantly decreased on the argon processed sample. But considering the compositional change, a sharper interface must be expected instead, since oxide formation is temporally much more limited than on the untreated sample which had been stored in air for a long time. Hence, rather micro-roughness is suggested to determine the interface sharpness in that case. The flattened slope of the argon processed sample is in good agreement with the high micro-roughness obtained by the PSD analysis.

With the addition of oxygen to the argon process gas or in operation with pure oxygen gas, the surface oxide layer increases up to 13.0 nm. The native oxide layer thickness is thus exceeded remarkably. Hence, an oxygen ion-induced surface oxidation process has to be considered. Furthermore, after pure oxygen processing, the interface sharpness is significantly enhanced. Despite the fact that the micro-roughness is slightly higher than for an untreated aluminium sample (table 2), the interface sharpness is more than doubled (table 3). Thus, the compositional abruptness is evidently improved during ion beam machining with oxygen operating gas. Continuitive experiments with oxygen gas, including erosion depths up to 2 μm , indicate a stagnancy of the oxide thickness at (13 ± 2) nm.

To analyse the tendencies within the oxide stoichiometry, the O_2^- signal was monitored additionally to the AlO^- signal. AlO^- ions are generated within the whole stoichiometry range, while O_2^- ions can be preferentially expected under compositions of oxygen excess. Hence, the $\text{O}_2^-/\text{AlO}^-$ signal ratio has been used to monitor qualitative changes in the stoichiometry characteristics (figure 7). As a general trend for all depth profiles, a higher oxygen content is found at the free oxide surface (depth = 0 nm). With increasing depth the oxygen content decreases until a more or less abrupt transition to the base line level at the oxide/aluminium interface appears. Note the large dynamic range over about two orders of magnitude measured at the oxygen-processed sample indicating the highest stoichiometry change. Furthermore, as already pointed out, instead of the O_2^- signal, the AlO^- signal is also sensitive to oxide compositions with low oxygen contents. As a result of the stoichiometry gradients in the $\text{O}_2^-/\text{AlO}^-$ signal ratios, the oxide/aluminium interface positions in the $\text{O}_2^-/\text{AlO}^-$ signal ratio plots are shifted by about 1–2 nm below the interface positions derived from the AlO^- signals.

The SIMS investigations further revealed an increased carbon signal within the oxide film (figure 7). The used ion source exhibits a graphite plasma anchor, which is in direct

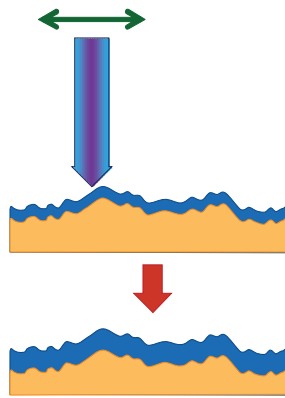


Figure 8. Model scheme of the RIBE machining process with oxygen. The oxygen ion beam is scanned over the aluminium surface initially exhibiting a native oxide layer. Due to oxygen ion implantation and chemical interaction a homogeneous and temporally stable, enhanced oxide layer is formed. This surface layer acts as a defined etch front moderating the inhomogeneous structural conditions of the aluminium bulk material. As a result, the topography degradation during depth machining is effectively impeded and the initial surface topography is almost preserved.

contact with the oxygen plasma. Compared to argon operation, the anchor erosion was enhanced due to oxygen processing.

3.4. The RIBE process model

Our results on the interaction of a low-energy oxygen ion beam with an aluminium surface suggest a particular erosion process model based upon the *in situ* formation of a surface oxide layer (figure 8). During ion beam treatment, this oxide is continuously eroded and simultaneously newly formed. Starting from the native Al_2O_3 surface layer, the oxide is firstly extended until a quasi-stationary oxide thickness is reached. At this point oxide erosion and formation compensate, while a distinct oxide composition profile between the free surface and the oxide/aluminium interface has evolved. This view is supported by the unchanged SIMS profiles obtained in the range of 0.5–2.0 μm depth machining, which is far from the initial oxide transformation process. The oxide covers the surface topography homogeneously with a constant thickness of about (13 ± 2) nm. The impact of energetic ions seems to be a necessary condition for the oxide formation, since the existence of molecular oxygen gas in the background gas is not sufficient to change to the process mode with reduced surface roughening. In contrast, domain-pattern structures are formed, also obtained by oxygen-free processing (figures 1 and 2). The increased roughening and domain-structure formation are affected by two aspects: (1) Aluminium has a comparatively low melting point of about 660 °C. Hence, a pure aluminium surface without surface oxide exhibits a high adatom mobility [36], and Ostwald-ripening of the differently oriented grains occurs. (2) The sputter erosion rate usually varies with respect to the grain orientation and compositional inhomogeneities additionally supporting the surface roughening. Both effects can be reliably faced by the chemical surface modification due to the impact of oxygen ions. Thus, the forming oxide layer is regarded as the key for smooth surface machining.

However, the insufficient supply of oxygen may result in an oxide layer which is not fully closed. This case can be especially expected for a rough surface, where the surface roughness is in the order or even more pronounced than the oxide thickness. As a result, during ion beam machining a self-masking effect has to be assumed allowing non-oxidized areas to be etched faster than oxidized areas. This situation can result in a much stronger surface roughening as observed for the $\text{Ar} : \text{O}_2(6 : 1)$ gas mixture (figure 5). Despite the fact that the oxide thickness obtained by SIMS is 11.3 nm (table 4) the oxide layer may not be fully closed. Moreover, there is no relevant benefit in the etch rate. In the face of the large excess of argon within the gas mixture, the etch rate was found to be already considerably reduced almost to the value of pure oxygen processing (table 2). The results suggest best surface properties in operation with pure oxygen gas rather than with an $\text{Ar} : \text{O}_2$ gas mixture. Based on this discussion, it may be considered that a strong initial surface roughness might be unfavourable for the preservation of the surface roughness during ion beam machining, and also with pure oxygen processing. To investigate such process limitations, further experiments will be necessary.

Also, in such related technological fields as reactive magnetron sputtering, the formation of a surface oxide layer on aluminium is considered [37]. However, the oxidation process of an aluminium surface by the assistance of oxygen ions is complex and currently not fully understood.

Under-stoichiometric AlO_x , i.e. with a decreased oxygen-content compared to Al_2O_3 stoichiometry, in the form of a homogeneous phase is thermodynamically not stable. Instead, phase separation to aluminium and Al_2O_3 is favored [38]. In the following, $\text{Al}_2\text{O}_3(x = 1.5)$ and two cases of under-stoichiometric AlO_x are discussed: $\text{Al} : \text{Al}_2\text{O}_3 = 2 : 1(x = 0.75)$ and $\text{Al} : \text{Al}_2\text{O}_3 = 4 : 1(x = 0.5)$. On the other hand, over-stoichiometric AlO_x phases, i.e. with excess oxygen, are only stable under static pressure. In particular, crystalline phases such as Al_4O_7 or AlO_2 become thermodynamically permitted [39]. In amorphous AlO_x high oxygen contents are common, already under thermodynamic standard conditions. Thus, AlO_x configurations with $x = 4$ and 5 near the aluminium substrate and $x = 6$ at the free oxide surface have been theoretically modeled and experimentally verified [40–42]. The amorphous structure is a build-up of densely packed oxygen atoms in a distorted fcc alignment, while the aluminium atoms occupy tetrahedral and octahedral interstitials [43]. Amorphous AlO_x can be favoured over a crystalline oxide phase on aluminium crystallites, especially in contact with less dense-packed lattice planes [44]. In oxides, the irradiation and implantation of energetic ions, as in the case of ion beam machining, usually results in the amorphisation of a thin near-surface film. In materials retaining crystallinity, as is typically the case for metals, lattice defects, predominantly vacancies and dislocations, are introduced. Furthermore, as a result of the incorporated strain in the amorphous as well as crystalline material, thermodynamic non-equilibrium conditions can be attained by ion irradiation. Hence, the formation of non-stoichiometric AlO_x has to be considered for modeling the RIBE machining process.

Table 4. Implantation ranges of 1.5 keV oxygen ions after normal impact onto thick oxide with respect to oxide composition derived from simulations with the SRIM-2008 and the TRIM.SP code. The spread ranges cover 95% of the ion distribution (2σ).

Oxide composition	Density (g cm ⁻³)	Ion implantation ranges			
		Mean depth (nm)	Depth spread (nm)	Lateral spread (nm)	
AlO ₆	2.38	5.2	±5.4	±6.7	SRIM-2008
		5.0	±5.2	±6.5	TRIM.SP
AlO ₅	2.49	5.0	±5.2	±6.6	SRIM-2008
		4.8	±5.0	±6.3	TRIM.SP
AlO ₄	2.64	4.7	±4.8	±6.3	SRIM-2008
		4.6	±4.8	±6.0	TRIM.SP
AlO ₃	2.91	4.3	±4.4	±5.8	SRIM-2008
		4.2	±4.4	±5.6	TRIM.SP
AlO ₂	3.43	3.8	±4.0	±5.1	SRIM-2008
		3.6	±3.9	±5.0	TRIM.SP
Al ₂ O ₃	3.95	3.3	±3.4	±4.5	SRIM-2008
		3.2	±3.4	±4.4	TRIM.SP
Al : Al ₂ O ₃	3.12	4.3	±4.6	±6.2	SRIM-2008
(2 : 1)		4.3	±4.7	±6.2	TRIM.SP
Al : Al ₂ O ₃	2.95	4.7	±5.0	±6.7	SRIM-2008
(4 : 1)		4.6	±5.1	±6.8	TRIM.SP

Oxygen-rich aluminium oxide may further be stabilized by incorporated carbon [45]. Since carbon was found in the SIMS investigations, there might be some contribution in the formation of the surface oxide layer. However, carbon incorporation is treated more as an impurity issue and thus it is not accounted for in the process modelling in this study.

The ion-surface interaction was analysed by the Monte Carlo simulation codes SRIM-2008 and TRIM.SP. However, both program codes do not cover the following experimental circumstances: (1) As a rude approximation, the solid is assumed as fully isotropic and amorphous matter. In particular, crystallographic effects, such as preferential sputtering of specific crystal orientations or ion channelling, are neglected. (2) The surface is treated as an ideal flat surface; surface topography or roughness are not considered. Hence, the experimentally verified surface roughening cannot be covered by the simulations. (3) Dynamical changes of the material composition or the formation of compositional gradients as indicated by the SIMS experiments are not included. (4) The effect of vacancy recombination is not considered. (5) Volume diffusion is not implemented. Despite these serious drawbacks, implantation profiles into homogeneous materials usually show a good agreement with the experiment. Furthermore, both codes allow for the calculation of sputter yield values. TRIM.SP delivers quite reliable results, while SRIM has been shown to differ from experimental values by up to a factor of 2 [46, 47]. Those deviations were also observed in this study. Hence, only the TRIM.SP sputter yields are discussed.

The ion implantation was simulated for the oxide layer/Al905 bulk system. In the initial state of oxygen ion beam machining the sample exhibits a thin native oxide film. Oxygen ions with 1.5 keV are implanted within the oxide, but considerable portions are not sufficiently dragged to prevent penetrating a few nm into the aluminium material as well (figure 9(a)). Hence, the oxide layer/aluminium interface progresses

in depth and the oxide composition profile alters. However, the particular dynamics are not accessible by the simulations. Nevertheless, the general effect of the oxide composition on the sputtering process can be evaluated, thus giving further insights into the principle interaction processes. As a result of the SIMS experiments, the oxide layer thickness extends in the initial stage of ion beam processing. Applying the ultimate oxide thickness of about 13 nm to the simulations the oxygen implantation is found to be concentrated almost in the oxide layer for all oxide compositions considered (figure 9(b)/(c)).

The effect of the oxide composition was further analysed by oxygen ion implantation simulations into oxide material only. As a result, the ion implantation depth varies between 3.2–5.2 nm with a spread (also called straggling) of 3.4–5.4 nm (table 4). In Al₂O₃ about 95% of the impinging oxygen ions are implanted within a depth up to 6.7 nm from the surface. This maximum implantation depth is far from the oxide thickness of 13.0 nm as measured by the SIMS experiments. However, at high stoichiometry deviations from the Al₂O₃ composition, i.e. for high contents of either aluminium or oxygen, the maximum oxygen implantation depth increases. The implantation ranges for Al : Al₂O₃ (4 : 1) up to about 9.7 nm and for AlO₆ up to 10.2–10.6 nm. Additional kinetic effects which further increase the oxide layer thickness as oxygen and aluminium diffusion can usually be neglected at room temperature conditions [48]. However, diffusion may be enhanced by vacancies formed during ion irradiation.

To approximate the actual oxide composition being formed during ion beam machining, experimental sputter yield values were estimated and compared to the simulated values. The experimental values were derived from a rough balance calculation between the implanted oxygen ions and the eroded amount of material. Based on the Faraday cup measurements, the oxygen ion beam fluence after 1 h of operation was evaluated to be 1.53×10^{19} cm⁻². The etching depth was

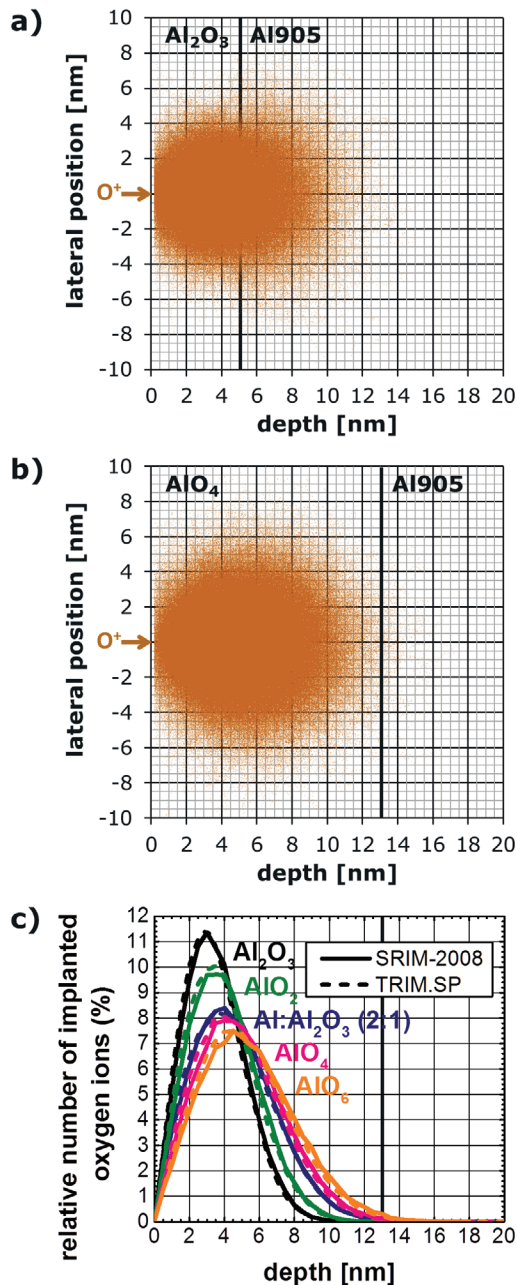


Figure 9. (a), (b) Ion trajectories after normal impact of 1.5 keV oxygen ions onto an oxide layer/Al905 bulk sample system calculated by SRIM-2008, and (c) corresponding implantation depth profiles calculated by SRIM-2008 and TRIM.SP. (a) The Al_2O_3 layer thickness of 5 nm corresponds to the initial situation of a native oxide layer at the beginning of ion beam machining. (b) Under quasi-stationary equilibrium conditions, a non-stoichiometric AlO_x layer with a thickness of 13 nm is formed (depicted here: $x = 4$). (c) The higher the stoichiometric deviation from the Al_2O_3 composition, i.e. for oxygen excess as well as deficit, the higher the oxygen implantation depth. In all considered cases the oxygen ions are implanted almost completely inside the oxide layer.

about 380 nm, which corresponds to an aluminium removal of $2.35 \times 10^{18} \text{ cm}^{-2}$. Note, the aluminium amount necessary to build up a 13.0 nm thick layer of $\text{Al}:\text{Al}_2\text{O}_3 = 2:1$ out of 5.7 nm Al_2O_3 adds up to $3.61 \times 10^{16} \text{ cm}^{-2}$, while for AlO_4 an excess of $3.85 \times 10^{15} \text{ cm}^{-2}$ aluminium persists. However, compared to

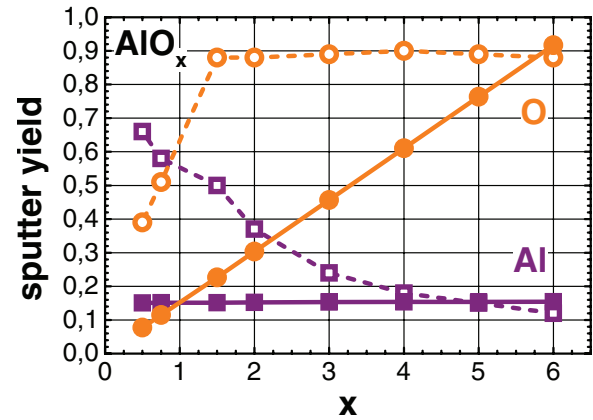


Figure 10. Sputter yields for the oxide components with respect to AlO_x composition as simulated by TRIM.SP for 1.5 keV oxygen ions with normal incidence (dashed lines/open symbols). For comparison, estimated sputter yield values from the RIBE experiments with oxygen gas are given (straight lines/full symbols). The aluminium values are determined directly from the material balance calculation, while the oxygen values are derived presuming the respective oxide composition.

the overall aluminium removal, those variations are marginal and the sputter yield of aluminium is about 0.15 aluminium atoms per incoming oxygen ion without a significant effect of the oxide composition (figure 10). Instead, the sputter yield of oxygen is strongly related to the oxide composition. Based on the view of a quasi-stationary etch front with constant composition profile and thickness, the experimental oxygen sputter yield values in figure 10 are calculated from the aluminium removal with the necessary condition that the respective oxide composition does not change during sputtering. Between an aluminium excess oxide such as $\text{Al}:\text{Al}_2\text{O}_3 = 4:1$ and an oxygen-enriched composition such as AlO_6 , the sputtered oxygen amount varies between 1.18×10^{18} – $1.41 \times 10^{19} \text{ cm}^{-2}$ resulting in a broad sputter yield range of 0.077–0.92 oxygen atoms per incoming oxygen ion. These values already include the oxygen amounts necessary to form the oxide layer for each composition. At the utmost $5.11 \times 10^{16} \text{ cm}^{-2}$ oxygen is needed for oxide build-up. In advance of the experimental sputter yield evaluation, the TRIM.SP code was applied for sputter yield simulation (figure 10). With increasing oxygen content in the oxide the sputter yield of aluminium decreases gradually. In contrast, the oxygen sputter yield increases from aluminium-rich to Al_2O_3 composition very steeply until it reaches a value of about 0.9 oxygen atoms per incoming oxygen ion. For higher oxygen contents, the oxygen sputter yield remains at this value. The comparison between the experimental and the simulated sputter yield curves in figure 10 reveals an excellent matching for a high oxygen content x of about 6. Moreover, the oxygen sputtering yield of 0.92 oxygen atoms per incoming oxygen ion is in reasonable agreement with the claimed material balance between the number of implanted oxygen ions and the number of removed oxygen atoms in a quasi-stationary dynamics.

In order to identify the responsible depth range at the oxide surface from which sputtering occurs, the sputtering yields of aluminium and oxygen were analyzed with respect

to the oxide thickness in a continuative simulation study. At a very low oxide thickness, sputtering results not only from the oxide film but also from the adjacent aluminium bulk material. However, beyond a thickness of 1.0 nm, the sputtering contribution from the aluminium bulk is sunk to 1% of the overall sputtered atoms. Conversely, it can be stated that sputtering from the oxide occurs only from the near-surface range until a depth of 1.0 nm. Hence, the oxide composition at the surface is decisive for the elemental sputter yields obtained. Since a compositional gradient is indicated by the SIMS measurements, the high oxygen composition of $x = 6$ has to be considered only in this localized surface region. This view is in good agreement with related surface oxide studies [40–42].

4. Conclusion

In summary, we examined a RIBE-based surface figuring technique based upon oxygen process gas. Compared to standard argon IBF processing the surface topography is exceedingly well preserved. Hence, the initial topography mostly determines the surface quality after ion beam processing. For the oxygen RIBE process the PSD analysis showed that shape and waviness between $0.0035\text{--}0.1\ \mu\text{m}^{-1}$ are largely preserved. An improvement of the surface topography was found for the turning mark features, which are smoothed out to some extent during ion beam machining. Residual surface degradation is caused by etch pit formation in the mid spatial frequency range between $0.1\text{--}10\ \mu\text{m}^{-1}$. The precipitate structures within the aluminium alloy matrix were identified as the origin. Al905 was found to exhibit a smaller pit size than obtained on Al6061. Hence, even less surface roughening was observed on Al905. In the high spatial frequency range of $10\text{--}20\ \mu\text{m}^{-1}$ the topography is degraded to some extent.

Based upon SIMS measurements and Monte Carlo simulations, a model view on RIBE machining with oxygen process gas is proposed. By the impact of energetic oxygen ions a laterally homogeneous and temporally stable oxide layer with a thickness of about 13 nm is formed. The AlO_x layer exhibits a composition profile with excess oxygen at the free surface and a gradual decrease of the oxygen content towards the oxide/aluminium interface. Sputtering is expected to originate from the 1.0 nm thick near-surface region. Based upon material balance calculations and simulated sputter yields by TRIM.SP, an oxygen-content of $x = 6$ is expected in this region. In accordance with the simulation results the experimental data reveal an aluminium sputter yield of 0.15 and an oxygen sputter yield of 0.92 for 1.5 keV oxygen ions impacting aluminium at normal incidence. The oxygen ions are completely implanted inside the oxide layer. As a result of continuous sputter erosion and simultaneous oxide formation by ion implantation, a quasi-stationary oxide thickness develops. The experimentally verified temporal stability is supported by the magnitude of the oxygen sputter yield in the order of 1, thus completely compensating the oxygen ion implantation. The chemical modification of the aluminium by oxidation suppresses the influence of the structural matrix effects on the sputter erosion

process efficiently. Hence, the oxide layer acts as a moderating etch front.

From a technological point of view, RIBE machining of aluminium with oxygen gas is a rather slow process with an etch rate about 4–5 times smaller than argon IBF. However, the significantly improved surface quality compared to conventional IBF now enables the direct figure error correction of optical aluminium surfaces without additional surface coatings. Moreover, RIBE machining is stable and clean without any hazardous by-products, making the process suitable for such applications [22].

Acknowledgments

The authors are very grateful to A Gebhard and R Steinkopf (Fraunhofer IOF) for the supply of the diamond-turned aluminium samples, to I Herold and T Liebeskind for sample preparation, to D Hirsch for SEM-EDX and support in the SIMS measurements, to A Nickel for providing the software tool for isotropic PSD calculation, to F Pietag for control logic support and valuable technological suggestions, and to H Paetzelt for the perusal of the manuscript.

Financial support by the German Federal Ministry of Education and Research (BMBF) within the framework of the InnoProfile Transfer initiative 03IPT706X ‘Ultra-precision manufacturing using atomic particle beams’ is gratefully acknowledged.

References

- [1] Weiser M 2009 *Nucl. Instrum. Methods Phys. Res. B* **267** 1390–3
- [2] Vukobratovich D and Schaefer J P 2011 Large stable aluminum optics for aerospace applications *Proc. SPIE* **8125** 81250T
- [3] Li L and Yi A Y 2010 *J. Opt. Soc. Am. A* **27** 2613–20
- [4] Li L and Yi A Y 2012 *Appl. Opt.* **51** 1843–52
- [5] Arnold T, Böhm G, Fechner R, Meister J, Nickel A, Frost F, Hänsel T and Schindler A 2010 *Nucl. Instrum. Methods Phys. Res. A* **616** 147–56
- [6] Fang F Z, Zhang X, Weckenmann A, Zhang G X and Evans C 2013 *CIRP Ann.—Manuf. Technol.* **62** 823–46
- [7] Taniguchi N and Kanekama N 1973 *Bull. Japan Soc. Precis. Eng.* **7** 29–30
- [8] Bigl F, Hänsel T and Schindler A 1998 *Vak. Forsch. Prax.* **10** 50–6
- [9] Hänsel T, Frost F, Nickel A and Schindler A 2007 *Vak. Forsch. Prax.* **19** 24–30
- [10] Gailly P, Collette J P, Jamar C, Fleury-Frenette K, Médart P and Stockman Y 2004 *Nucl. Instrum. Methods Phys. Res. B* **216** 206–12
- [11] Xie X, Zhou L, Dai Y and Li S 2011 *Appl. Opt.* **50** 5221
- [12] Liao W, Dai Y, Xie X and Zhou L 2014 *Opt. Express* **22** 377–86
- [13] Shanbhag P M, Feinberg M R, Sandri G, Horenstein M N and Bifano T G 2000 *Appl. Opt.* **39** 599–611
- [14] Frost F, Takino H, Fechner R, Schindler A, Ohi N and Nomura K 2007 *Japan. J. Appl. Phys.* **46** 6071–3
- [15] Peverini L, Kozhevnikov I V, Rommeveaux A, Vaerenbergh P V, Claustre L, Guillet S, Massonnat J Y, Ziegler E and Susini J 2010 *Nucl. Instrum. Methods Phys. Res. A* **616** 115–8

- [16] Wu L, Qiu K and Fu S 2016 *Nucl. Instrum. Methods Phys. Res. B* **370** 79–85
- [17] Xu M, Dai Y, Xie X, Zhou L and Liao W 2015 *Appl. Opt.* **54** 8055–61
- [18] Eger C M 1992 Roughness evolution of optical materials induced by ion-beam milling *Proc. SPIE* **1752** 63–72
- [19] Steinkopf R *et al* 2008 Metal mirrors with excellent figure and roughness *Proc. SPIE* **7102** 71020C
- [20] Folkman S L and Stevens M 2002 Characterization of electroless nickel plating on aluminum mirrors *Proc. SPIE* **4771** 254–64
- [21] Gebhardt A, Kinast J, Rohloff R R, Seifert W, Beier M, Scheiding S and Peschel T 2014 Athermal metal optics made of Nickel plated AlSi40 *Int. Conf. Space Optics (Tenerife, Canary Islands)*
- [22] Arnold T and Bauer J 2016 Ion beam figuring of RSA aluminium surfaces *16th Int. Conf. European Society for Precision Engineering and Nanotechnology* ed P Bointon *et al* (Nottingham: EUSPEN) p O3.4
- [23] Donnelly V M and Kornblit A 2013 *J. Vac. Sci. Technol. A* **31** 050825
- [24] Gubbels G, Tegelaers L and Senden R 2013 Melt spun aluminium alloys for moulding optics *Proc. SPIE* **8884** 88841W
- [25] Newswander T, Crowther B, Gubbels G and Senden R 2013 Aluminum alloy AA-6061 and RSA-6061 heat treatment for large mirror applications *Proc. SPIE* **8837** 883704
- [26] Ziegler J, Biersack J and Ziegler M 2008 *SRIM-the Stopping and Ranges of Ions in Matter* (Chester: SRIM Co.)
- [27] Eckstein W 1991 *Computer Simulation of Ion-Solid Interactions* (Berlin: Springer)
- [28] Ziegler J F, Biersack J P and Littmark U 1985 *The Stopping and Range of Ions in Matter* vol 1 (New York: Pergamon)
- [29] Wilson W D, Haggmark L G and Biersack J P 1977 *Phys. Rev. B* **15** 2458–68
- [30] Bernheim M and Slodzian G 1973 *Int. J. Mass Spectrom. Ion Phys.* **12** 93–9
- [31] Sproul W D, Christie D J and Carter D C 2005 *Thin Solid Films* **491** 1–17
- [32] Chakrabarti D J, Cheong B K and Laughlin D E 1998 Precipitation in Al–Mg–Si–Cu Alloys and the role of the Q-phase and its precursors *Automotive Alloys II* ed S K Das (Warrendale, PA: The Minerals, Metals & Materials Society) pp 27–44
- [33] Harvey J E and Thompson A K 1995 Scattering effects from residual optical fabrication errors *Proc. SPIE* **2576** 155–74
- [34] Duparré A, Ferre-Borrull J, Gliech S, Notni G, Steinert J, Bennett J M J, Gilech S, Notni G, Steinert J and Bennett J M J 2002 *Appl. Opt.* **41** 154–71
- [35] Frost F, Fechner R, Ziberi B, Völlner J, Flamm D and Schindler A 2009 *J. Phys.: Condens. Matter* **21** 224026
- [36] Nakhodkin N and Shaldervan A 1972 *Thin Solid Films* **10** 109–22
- [37] Kuschel T and von Keudell A 2010 *J. Appl. Phys.* **107** 103302
- [38] Wriedt H A 1985 *Bull. Alloy Phase Diagr.* **6** 548–53
- [39] Liu Y, Oganov A R, Wang S, Zhu Q, Dong X and Kresse G 2015 *Sci. Rep.* **5** 9518
- [40] Iijima T, Kato S, Ikeda R, Ohki S, Kido G, Tansho M and Shimizu T 2005 *Chem. Lett.* **34** 1286–7
- [41] Hasnaoui A, Politano O, Salazar J M and Aral G 2006 *Phys. Rev. B* **73** 1–13
- [42] Hattori S, Kalia R K, Nakano A, Nomura K I and Vashishta P 2012 *Appl. Phys. Lett.* **101** 1–4
- [43] Jeurgens L P H, Sloof W G, Tichelaar F D and Mittemeijer E J 2002 *Surf. Sci.* **506** 313–32
- [44] Jeurgens L P H, Sloof W G, Tichelaar F D and Mittemeijer E J 2000 *Phys. Rev. B* **62** 4707–19
- [45] Cuffe R, Baud G, Benmalek M, Besse J P, Butruille J R and Jacquet M 1996 *Surf. Coat. Technol.* **80** 96–9
- [46] Wittmaack K 2004 *J. Appl. Phys.* **96** 2632
- [47] Hofsäss H, Zhang K and Mutzke A 2014 *Appl. Surf. Sci.* **310** 134–41
- [48] Paladino A E and Coble R L 1963 *J. Am. Ceram. Soc.* **46** 133–6